# Supporting Information

## Triboelectrification: Backflow and Stuck Charges are Key

Hyunseok Ko†, Yeong-won Lim†, Seungwu Han, Chang Kyu Jeong*, Sung Beom Cho*

**AUTHOR INFORMATION**

**Corresponding Authors**

**Sung Beom Cho** - Convergence Technology Division, Korea Institute of Ceramic Engineering and Technology (KICET), Jinju, Gyeongsangnam-do, 52851, Republic of Korea; Email: csb@kicet.re.kr

**Chang Kyu Jeong** - Division of Advanced Materials Engineering, Jeonbuk National University, Jeonju, Jeollabuk-do, 54896, Republic of Korea; Department of Energy Storage/Conversion Engineering of Graduate School & Hydrogen and Fuel Cell Research Center, Jeonbuk National University, Jeonju, Jeollabuk-do, 54896, Republic of Korea; Email: ckyu@jbnu.ac.kr

**Authors**

**Hyunseok Ko** - Research Institute of Advanced Materials, Seoul National University, Seoul, 08826, Republic of Korea; Convergence Technology Division, Korea Institute of Ceramic Engineering and Technology (KICET), Jinju, Gyeongsangnam-do, 52851, Republic of Korea

**Yeong-won Lim** - Division of Advanced Materials Engineering, Jeonbuk National University, Jeonju, Jeollabuk-do, 54896, Republic of Korea; Department of Energy Storage/Conversion Engineering of Graduate School & Hydrogen and Fuel Cell Research Center, Jeonbuk National University, Jeonju, Jeollabuk-do, 54896, Republic of Korea

**Seungwu Han** - Research Institute of Advanced Materials, Seoul National University, Seoul, 08826, Republic of Korea; Department of Materials Science and Engineering, Seoul National University, Seoul, 08826, Republic of Korea

† These authors contributed equally to this work.

Complete contact information is available at: https://pubs.acs.org/

## SI Methods

### Methods 1: Fabrication of contact-separation mode TEGs

$Al_2O_3$, MgO, $LaAlO_3$, $SrTiO_3$, and $TiO_2$ (Rutile) single crystal wafers (1 cm × 1 cm, 0.5 mm thick) were purchased from Madelab Co. (Table S1). Au film (~300 nm thick with Cr adhesion (10 nm)) was deposited by an evaporator on a quartz substrate to prepare electrodes. Au was used not only as a top electrode, but also as the counterpart triboelectric surface material. In addition to the single crystal wafer feature, all samples were treated and cleaned using a buffered oxide etchant (BOE) solution to minimize surface roughness. Al was deposited as the bottom electrode on the backside of $Al_2O_3$, MgO, $LaAlO_3$, $SrTiO_3$, and $TiO_2$ wafers for the sole purpose of signal measurements (i.e., not related to triboelectric charging phenomena at the interface). Cu wires were attached to each electrode using conductive epoxy to connect the measuring equipment. The real TEG device used in experiment is shown in Figure S1. The TEG devices were made of each single-crystal oxide wafer and the counterpart Au film deposited on a supporting substrate with the size of 10 mm × 10 mm. The gap between the two triboelectric surfaces was set up as 5 mm because it was efficient for triboelectric signals as reported previously.[1]

### Methods 2: Triboelectric output measurement of TEGs

All TEG devices were placed between the jig and the bottom floor plate in a pressing stage to measure triboelectric voltage and current output generated from contact electrification. The pressing state was constructed in a Faraday cage to eliminate other artifacts from the environment. The initial distance between the metal film surface (attached on the jig) and the dielectric wafer surface (attached on the bottom floor plate or heating plate) was fixed at 5 mm. The frequency of contact-separation motion was 1.4 Hz and the applied force was 50 N with a jig velocity of 0.1 m/s as the optimized operating conditions of the pressing machine. The area

of the TEG devices was 1 $cm^2$, thus an input pressure is 0.5 MPa. The open-circuit voltage, short-circuit current, and charge density signals of the TEGs were measured with a Keithley 6514 electrometer and data acquisition (DAQ) system with real-time recording.

In addition to the Faraday cage, environmental conditions were also controlled by a thermo-hygrostat and an air purifier. The room temperature (298 K) and relative humidity < 20% were maintained. For the temperature-dependent experiments, a heating plate was placed between the bottom floor plate and dielectric specimen, which could be heated to the desired temperature (up to 483 K). All experiments were conducted under the ambient pressure with low humidity in a cleanroom. Although gas atmosphere or pressure level may affect the absolute amount of electron transfers, it is not associated with the relative tendency of triboelectric series.[2-3] It should be noted that the electron transfer is important in the triboelectrification of dielectrics-metal pairs. Hence, the ambient atmosphere and pressure does not affect the tendency of triboelectric series in the material system of five oxides and metal for our theoretical approaches.

**Methods 3: First-principles calculations**

All DFT calculations were performed with the Vienna Ab-Initio Simulation Package (VASP).[4] VASP calculations were performed using the projector-augmented plane-wave (PAW) method [5-6] and the generalized gradient approximation (GGA) exchange-correlation potentials, parameterized by Perdew, Burke, and Ernzerhof (PBE).[7] The energy cut-off was set as 520 eV, the Brillouin zone was sampled with a gamma-centered 3 × 3 × 1 mesh, and a 7 × 7 × 1 mesh was used for electronic structure calculations. Periodic boundary conditions were employed, and dipole corrections [8] were made to correct the effect of the electric dipole on the surface of the finite cell. Bader charges were evaluated to quantify charge transfer across the interface.[9]

**SI Notes**

**Note 1. Work function of Au**

The work function of metal is an important value to ascribe the electron behavior in metal. Au used in our experiment is sputtered, thus it does not have clear orientation. To examine the work function (WF) difference depending on crystal orientation, thus we have calculated Au work function here. WFs for three Au slabs are calculated, (1 0 0), (1 1 0) and (1 0 $\bar{1}$), and the values were found as 5.09, 5.18, and 5.01 eV, respectively. The work function difference for different orientations are found to deviate less than 2% of experimental value of 5.1 eV.[10] Hence, the significance of Au orientation on WF is neglected in the discussion.

**Note 2. Surface state of dielectrics**

In principle, the surfaces of dielectrics are presumed to be oxygen-terminated. For the (0 0 1) perovskite structures, transition metal oxide layer (LaO, SrO) terminated is considered. At ambient condition, the surfaces of ceramics are occasionally hydroxylated because of the high surface free energy owing to the dangling bonds. Herein we have determined realistic surface of dielectrics according to the surface stability of hydrogen in literature, and calculated surface free energy if necessary. The stable surface state of α- $Al_2O_3$ has been reported to be hydroxylated with full coverage.[11-12] In a supercell, the oxygen-terminated surface is hydroxlated with H atoms on top of the oxides, and hydrogen layer and first two layers α-$Al_2O_3$ are relaxed. Hydroxylation on perovskite structures, $LaAlO_3$ [13] and $SrTiO_3$ [14], are endothermic at all coverages thus the bare surface is stable. For MgO and $TiO_2$, we have calculated the surface free energy ($E_{surf}$) at different H coverage, as shown in Figure S2a. $E_{surf} = \gamma_{surf} + \frac{(E_{slab,H} - E_{slab} - n\mu_H)}{2A}$ (S. 1)

where the $\gamma_{surf} = \frac{(E_{slab} - E_{bulk})}{2A}$ is the surface energy, and $E_{bulk}$, $E_{slab}$ and $E_{slab,H}$ are system energies of bulk, slab, and slab with surface hydroxylation, respectively. The value of

3.39 eV is used for $\mu_H$ at ambient condition, which agrees with Silveri *et al*.[15] As it can be seen, the bare surface is found most stable surface configuration for both MgO and $TiO_2$.

As elaborated, only $Al_2O_3$ in this study is hydrogen (H)-passivated. The surface H can facilitate additional charge transfer, namely by ion (material) transfer. The H atoms can unbind from surface of $Al_2O_3$ and transferred to metal surface, accompanying charge with them. To assess how easily H atoms unbinds, the binding energy of single H from $Al_2O_3$ surface with different initial H coverage is calculated and Shown in Figure S2b. For high coverage, greater than 93%, the unbinding of H is exothermic, but becomes endothermic reaction below that coverage. Although the quantitative contribution of charge transfer is minute due to the low concentration of unbind H atoms, the charge transfer can be indeed facilitated ionic transfer. Such subsidiary mechanism may have attributed to the discrepancy observed between $W_{calc}$ and $W_{exp}$ observed in Figure 3c.

**Note 3. Atomic structure and interface**

The epitaxial match between Au and dielectric systems were optimized. The epitaxy is chosen to balance the size of computational cell and the lattice mismatch. The selected crystal group and orientations are used in the experiments in parallel. For the chosen orientations, the surface states of dielectrics were either hydroxylated or clean as shown in Table S1, depending on the surface phase diagram of each system. Each dielectric slabs are then relaxed at fixed volume where every atom was converged within 0.05 eV $Å^{-1}$. The interface with Au is then generated using a total of 6 layers Au. The number of layers for dielectrics are determined differently for different system. The number of layers was set to avoid undesired out-of-plane polarization effect; thus the dielectric slabs were symmetry along the center plane that is perpendicular to the surface. The total cell size perpendicular to the surface is set as 50 Å, to ensure a sufficient vacuum thickness even when two materials are taken apart (i.e. vacuum thickness > 15 Å, for

all cases). The distance between the Au and dielectric surfaces changed ranging from 1.5 to 8 Å.

**Note 4. Equilibrium separation distance and system energy**

The system of two materials apart with separation distance, *d*, will experience attraction and repulsion which are caused by atomic interaction and surficial energy. The energy of such system does reduce while two materials getting closer (reducing surface energy), reaches equilibrium at some distance, and increases when they are even closer due to the atomic repulsion. According to the relationship between force and potential, the equilibrium separation distance, $d_{eq}$ is defined as $\left|\frac{dE}{dz}\right|_{d=d_{eq}} = 0$. The energies of Au-dielectric systems are shown in Figure S3. The total system energy reaches a minimum value when $d_{eq}$=2.0 – 2.5 Å. The systems have no interactions at $d_{eq} \geq 7$ Å, as there energy is equivalent to the energy of infinitely separated system energy with differences less than 0.1 %.

Here we demonstrate the distance between two materials cannot be closer than the equilibrium distance. For $d > d_{eq}$, the system is in the attraction regime thus there is no significant force exerted. For $d < d_{eq}$, the system is in the compulsion regime and the energy is required for two system to become closer. Assume that the two materials are separated by 0.1 Å closer than $d_{eq}$, one can compare the experimentally exerted work and the theoretical required energy from $d = d_{eq}$ to $d = d_{eq} - 0.01$ Å . The work done to the system of unit surface area (50 × 50 mm$^2$) can be calculated by the relation of $V_{comp} = F\Delta d_z$, where the $F$ is the applied compressive force exerted which was set as 50 N and the $\Delta d_z$is the trajectory length of the force exerted. Then $V_{comp}$ is $50\ \text{N} \times 0.01\ \text{Å} = 2.5 \times 10^{-9}$ J . For the $TiO_2$ system which has lowest $\frac{\partial \text{E}}{\partial d}$ at $d_{eq}$=2.5 Å, the change in system energy for 50 × 50 mm$^2$ is calculated as $9.2 \times 10^{-6}$ J (+ 0.1 eV for 43.4 Å$^2$). The exerted work done to the system is 3 orders of

magnitude lower than the energy required to put two materials 0.01 Å closer from the equilibrium distance. Thus, under current experimental setup, the distance between two materials is presumed to be no smaller than the equilibrium distance.

**Note 5. Viability of TE electron transfer mechanisms**

(I) Spatial charge redistribution model: Electron redistribution on the surface of contact materials can trigger the transfer of electrons across the interface.[16] When the surfaces of two materials approach one another, the electrons from each material begin to interact. Electron orbitals can spatially overlap, resulting in electron redistribution on the surfaces until a new thermodynamic equilibrium is reached.[16-18] The tailing wave function of metal surfaces either reflects or penetrates to reach this new equilibrium, termed the "compression effect".[18-19] When the materials are then separated, which is regarded as a non-equilibrium process at a given retrieval scale in experiments, the electrons are bound to the counter material, and are consequently transported.

Figure S4a is a schematic illustration showing the interface charge density with varying separation distance ($d$) in order to simulate the simple charge redistribution model (I). The amount of charge transfer is expected to decrease as $d$ increases because the electrostatic interaction between the two materials decreases and eventually becomes zero. The calculated interface charge densities ($\sigma^{intf}$) for different dielectrics are shown in Figure S4b. Bader charge analysis was employed to assess how the electrons are partitioned, and the $\sigma^{intf}$ was evaluated by summing up excess/depleted electrons on each side of the material. The dielectrics and Au are positively and negatively charged, respectively, with the same magnitude of charge. Since the interface charge density relies on the distance between the two materials, the atomic-scale distance upon mechanical contact should first be considered for the TE process under general contact-separation conditions. Comparing the energy from a mechanical compressive force and that of the Coulombic energy (SI Note 4), the distance at the mechanical contact between both

materials cannot be closer than the equilibrium distance ($d_{eq}$) because of the immense repulsive force between atoms. Hence, it is reasonable to assume that the distance between the Au film and the dielectric material becomes $d_{eq}$ upon full contact. Our analysis was based on the equilibrium state of the contact between the Au film and dielectric material at the interface separated by $d_{eq}$, which ranged from 2.0 to 2.5 Å (Figure S3). At the $d_{eq}$, the $\sigma^{intf}$ values are found on the order of $10^{-1}$ to $10^{0}$ C/m$^2$ (Figure S4b), with $Al_2O_3$ > $TiO_2$ > MgO > $LaAlO_3$ > $SrTiO_3$. It should be noted that the tendency of the theoretical computation disagrees with the experimentally observed trend. More importantly, the calculated charge density on the surfaces does not correspond to the scale of the experimentally measured charge density (the shaded region in Figure S4b); the calculated interface charge densities are 4-5 orders of magnitude higher than the experimental ones, which infers that the simple interface charge redistribution model does not solely account for the measured outputs.

(II) Surface state model: In the charge transfer process of dielectrics, free electrons are directly transferred from the valence band to metals by overcoming the bandgap. Nonetheless, extrinsic surface states can be created from interactions between the dielectric and the extrinsic source (i.e., metal counterpart).[20-21] Substantial density of states (DOS) at the surface may be present at the contact, as valence electrons can have a large influence from external sources such as chemical bonds.[21] Surface states have been demonstrated in photoemission studies, whereby a change in photon energies of chlorides[22] and polymers[23] was observed after contact. It is deduced that the surface states resulted from non-equilibrium dynamics can provide the driving force and determines the polarity in triboelectric initiation.[24]

As illustrated in Figure S4c, the surface state can be tribologically generated between the conduction and valence bands by mechanical contact, which enables electron transfer. Comparison of the DOS before and after contact was computed to examine the surface state in TE. In Figure S4d, the atom-decomposed partial DOS for two layers of the $Al_2O_3$-Au interface was used as a representative example because the $Al_2O_3$-Au pair showed the highest

triboelectric output in the aforementioned experiment. It should be noted that there is no distinctive $Al_2O_3$ surface state at the interface (Figure S4d, right) compared to the surface before contact (Figure S4d, left), regardless of minute changes. Similarly, the absence of surface states was confirmed for other material systems (Figure S5). Even though discrete surface states might exist under equilibrium[25] and non-equilibrium (e.g., strain[24] and flexoelectricity[26]) conditions, and when asymmetry occurs (e.g., surface roughness[27], defects[28], and bond polarity[29]) as a subsidiary mechanism, the basic absence of surface states at equilibrium excludes the surface state model (II) as a dominant electron transfer mechanism in TE.

(III) Effective work function change model: A typical approach to establish a driving force for electron transfer in metal-dielectric TE is facilitating band alignment at the heterojunction. At the hetero-interface, the Fermi levels of the metal and dielectric are aligned, and bending of the electronic bands is driven by an imbalance in charge neutrality or interface dipoles.[30-31] The work function adjacent to the interface (i.e., the effective work function) changes from the local vacuum level. In the theoretical computational study, it was stressed that both the charge transfer at the interface and the compressive electrostatic effect led to a change in the metal work function at the metal-dielectric interface,[19] and was experimentally shown that the change in the effective work function of various dielectric–metal systems depends significantly on the dielectric material.[32] Additionally, the effective work function can be modified by a shift in the relative band levels by intra-surface chemical bonding, [33] or by the bonding state of the surface atoms.[34]

A schematic illustration of the effective work function change model (III) is depicted in Figure S4e. Mechanical contact can induce Fermi level alignment, which then leads to immediate polarization of a few unit cells at the interface, resulting in variations of the local vacuum level across the interface. The effective work function ($\phi_{eff}^{intf}$), which is the work required to liberate an electron from the surface of dielectrics (with positive triboelectric charge), is then regarded as the difference between the local vacuum level of the metal and the

interface Fermi level, $\phi_{eff}^{intf} = E_{vacuum}^{metal} - E_F^{intf}$. The effective work function for the metal-dielectric contact at the equilibrium distance was calculated and is summarized in Figure S4f (energy band diagram before and after contacts are shown in Figure S6). The effective work function ranged from 2.85 to 6.03 eV, with the highest value obtained for the Au-$LaAlO_3$ pair. As calculated by first-principles, the relative order based on the work function change model does not coincide with the experimental results.

**Note 6. Numerical analysis of quantum tunneling**

The eigenvalues of wave function are numerically solved with time-independent Schrodinger equation. The eigenenergies are solved for the quasi bound states with open boundary conditions for outgoing waves at both ends of the modeling domain. The domains were set in 1D, 10 Å on each side of metal and dielectric, and the thickness of barrier is set as 2.5 Å, which was the median of the equilibrium distance found for five investigated system. The barriers are designed as finite-square-well, where the height of barriers are taken from DFT calculations. The stationary Schrodinger equation is

$$\hbar^2 \nabla \cdot \left(\frac{\nabla\psi(x)}{2m_{eff}(x)}\right) + V(x)\psi(x) = E\,\psi(x) \quad \text{(S. 2)}$$

where $m_{eff}$ is the effective mass, E is the total energy, $\hbar$ is a plank constant and the $V(x)$ is the potential energy which is set as following:

$$V(x) = 0\ (x < 0 \text{ or } x > 2.5) \quad \text{(S. 3a)}$$

$$V(x) = W\ (0 \le x \le 2.5\ ) \quad \text{(S. 3b)}$$

The $m_{eff}$ of metal and dielectric domains are set as 1.1 $m_e$ and 9.0 $m_e$ respectively, where $m_e$ is the mass of an electron $9.1 \times 10^{-31}$ kg. The probability density, $|\psi(x)|^2$, for each wave functions are computed, and an example of ~1.1 eV is shown in Figure S9a, whereby an electron from the metal tunnels through the barrier into the dielectric material (the backflow). The probability density ($\rho$) decreases as it passes through the potential barrier. Then the tunneling

probability is calculated as the ratio of integrated probability on dielectric bound to integrated probability on metal bound.

$$\frac{\int_{-\infty}^{0}|\psi(x)|^2 dx}{\int_{2.5}^{\infty}|\psi(x)|^2 dx} \quad \text{(S. 4)}$$

The tunneling probability as a function of the electron energies are evaluated for five systems and fitted to a simple exponential function ($a \cdot \exp(x-b)$), as shown in Figure S9b. The decency of fit indicates that the tunneling effect is a barrier-dependent exponential function, which explains the non-linear and positive relationship between the potential barrier and the triboelectric voltage/current output, further supporting the validity of the backflow-stuck charge model. The consequential tunneling probability (the ratio of the total probability on the dielectric to that on the metal) ranges from 0.2 to 10%, indicating a clear exponential functional. It should be mentioned that with more realistic barrier shape of Gaussian-like, the tunneling probability still followed exponential relation.

As above, we have demonstrated the non-linear correspondence of interface barrier and TE outputs. Additionally, the tunneling probability with respect to separation distance (*d*) is examined whether the exponential relation of TE outputs holds at every separation distance. The tunneling probability w.r.t. barrier thickness (i.e. separation distance), *d*, can be approximated in terms of electron energy (E) and the interface barrier (*W*):

$$P = \frac{16\mathrm{E}(W-\mathrm{E})}{W^2}\mathrm{e}^{-2kd} \quad \text{(S. 5)}$$

where $k$ is the wave number which is calculated as $k = \frac{2\pi}{h}\sqrt{2m_e(W-E)}$. As shown in Figure S10, regardless of the separation distance, the tunneling probabilty for electrons do follow exponential relation with the interface barrier.

## SI Tables

**Table S1.** Information of single-crystalline inorganic dielectric wafers used in the study. Crystal structure, crystal orientation of dielectrics and Au-pairs are listed. The surface states of dielectrics are ascribed in Supporting Information.

| Dielectric | Crystal | Ori.(di) | Ori.(Au) | Surface[a)] | Termination [a)] |
|---|---|---|---|---|---|
| $Al_2O_3$ | R3c (sapphire) | 0001 | 10-1 | H | - |
| MgO | Fm3m (rocksalt) | 110 | 110 | - | - |
| $LaAlO_3$ | Pm3m (perovskite) | 100 | 110 | - | La-terminated |
| STO | Pm3m (perovskite) | 100 | 110 | - | Sr-terminated |
| $TiO_2$ | P42/mnm (Tetragonal, Rutile) | 001 | 110 | - | - |

[a)]only considered for calculations

**SI Figures**

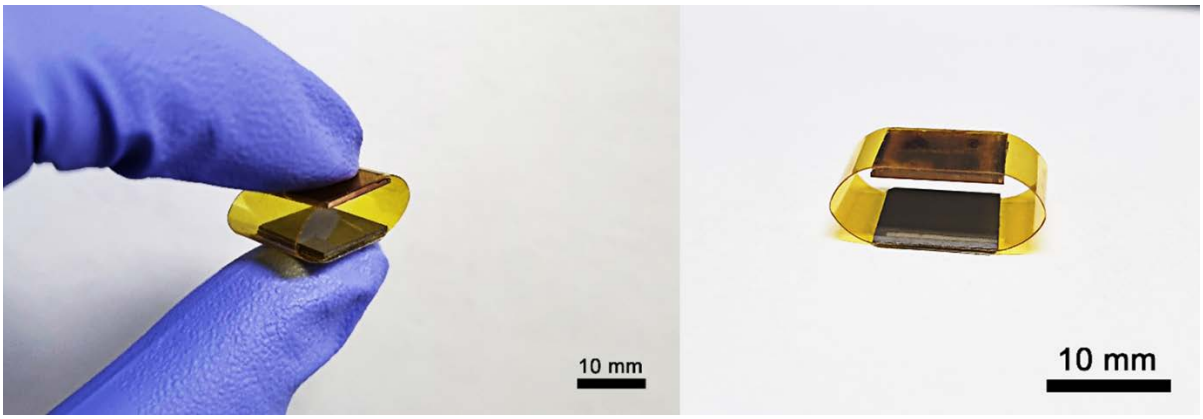


**Figure S1.** Photographs of a TEG device used in the experiment. The TEG consists of each single-crystal wafer and the counterpart Au metal film deposited on a carrier quartz substrate. The area is 10 mm × 10 mm. The two counterpart surfaces were linked by the fixture of elastic Kapton sheets. The gap between the surfaces controlled 5 mm, which can be set up in the pressing machine stage.

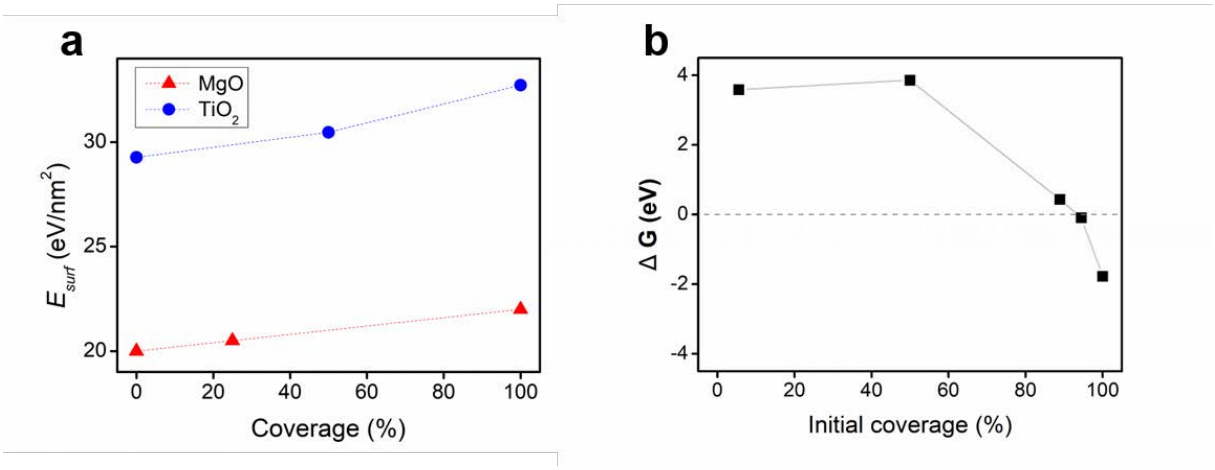


**Figure S2.** (a) The correlation between hydrogen coverage and surface free energy of the MgO and $TiO_2$ dielectric surfaces. (b) Hydrogen desorption energies on $Al_2O_3$ surface at varying surface coverage.

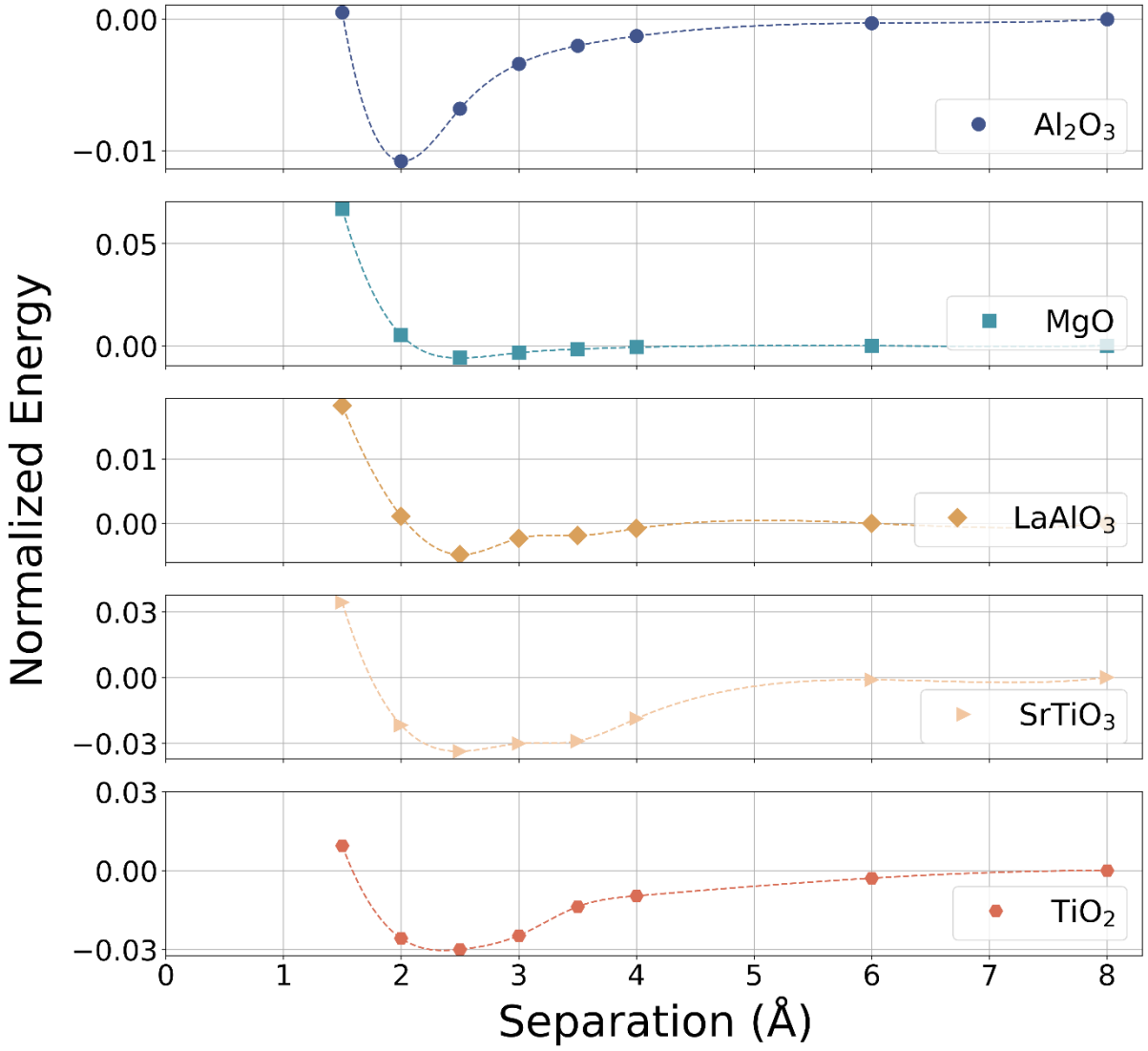


**Figure S3.** The DFT calculation results for the total energies of Au-dielectric systems as a function of separation distance. The energies are normalized with respect to the system energy with no interaction (i.e. infinitely apart).

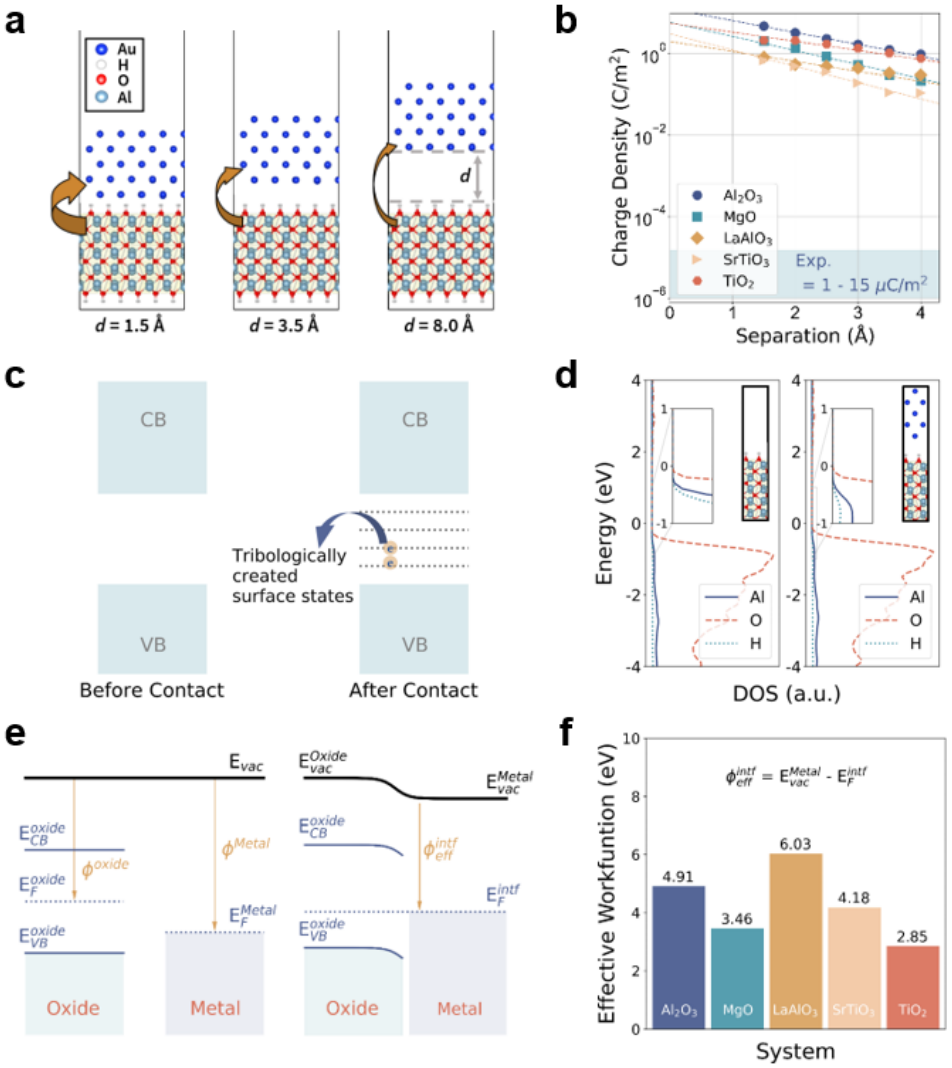


**Figure S4.** (a) Simulation schemes of the simple charge redistribution model by electron transfer at interfacial contacts between the dielectric material and metal at a separation distance, *d*. (b) Charge density on each dielectric slab obtained from first-principles calculations. The dashed lines are an exponential fitting of the simulated data. The shaded region indicates the magnitude of the experimentally obtained charge density. (c) Schematic of the surface bandgap state model showing the tribologically created surface electronic state on a given dielectric surface. (d) Element-decomposed DOS of the first two layers of the surface, where E = 0 eV is the valence band maximum. (e) Schematic of energy band diagrams for the metal and dielectric materials before (left) and after (right) contacts, illustrating the work function change model. (f) Triboelectric-induced effective work functions simulated by first-principles calculations in Au-dielectric systems at the equilibrium distance.

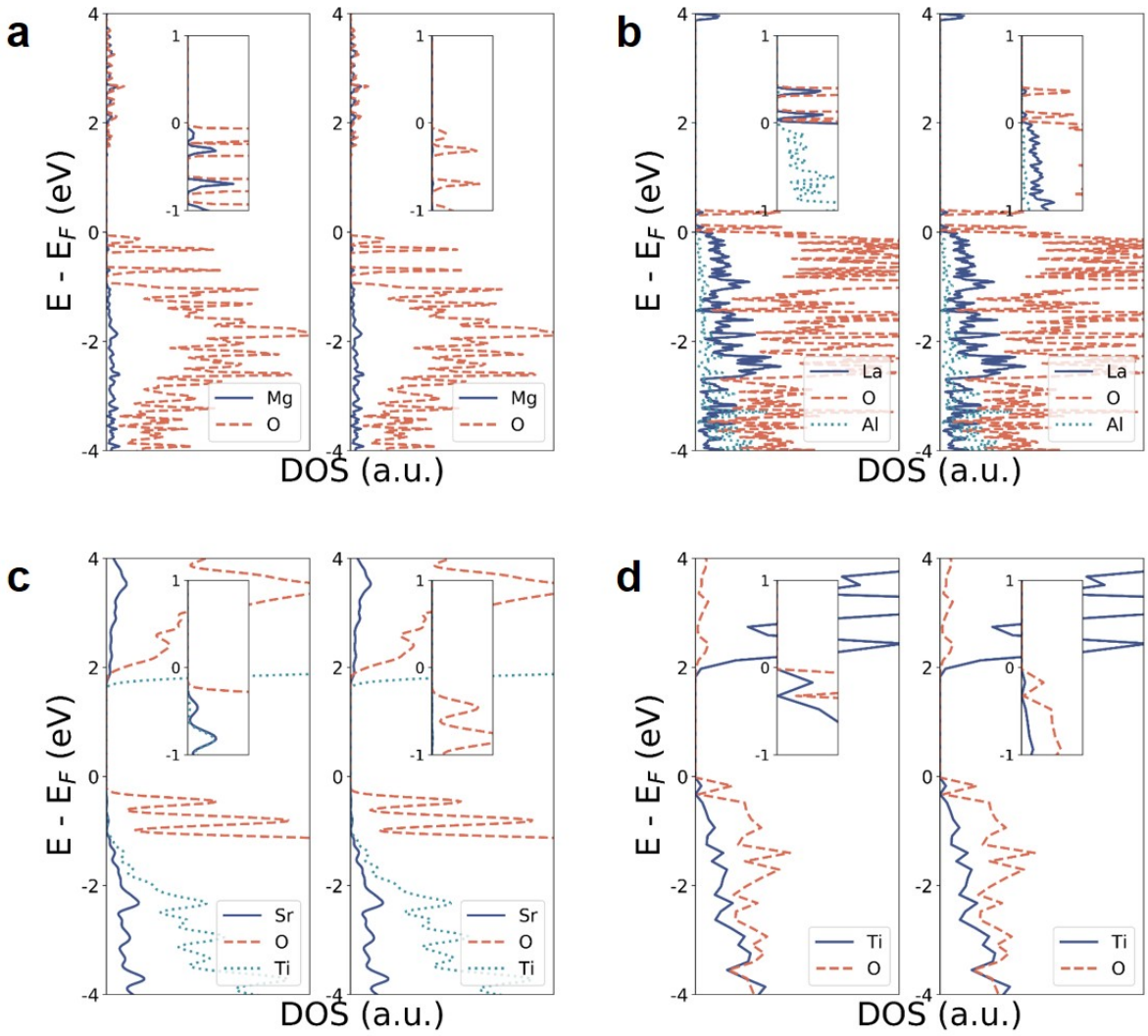


**Figure S5.** Density of state (DOS) calculated for Au-dielectric systems. (a-d) Element-decomposed DOS of surface atoms of dielectric slabs before (left panel) and after contact (right panel) with Au are shown for (a) MgO, (b) $LaAlO_3$, (c) $SrTiO_3$, and (d) $TiO_2$.

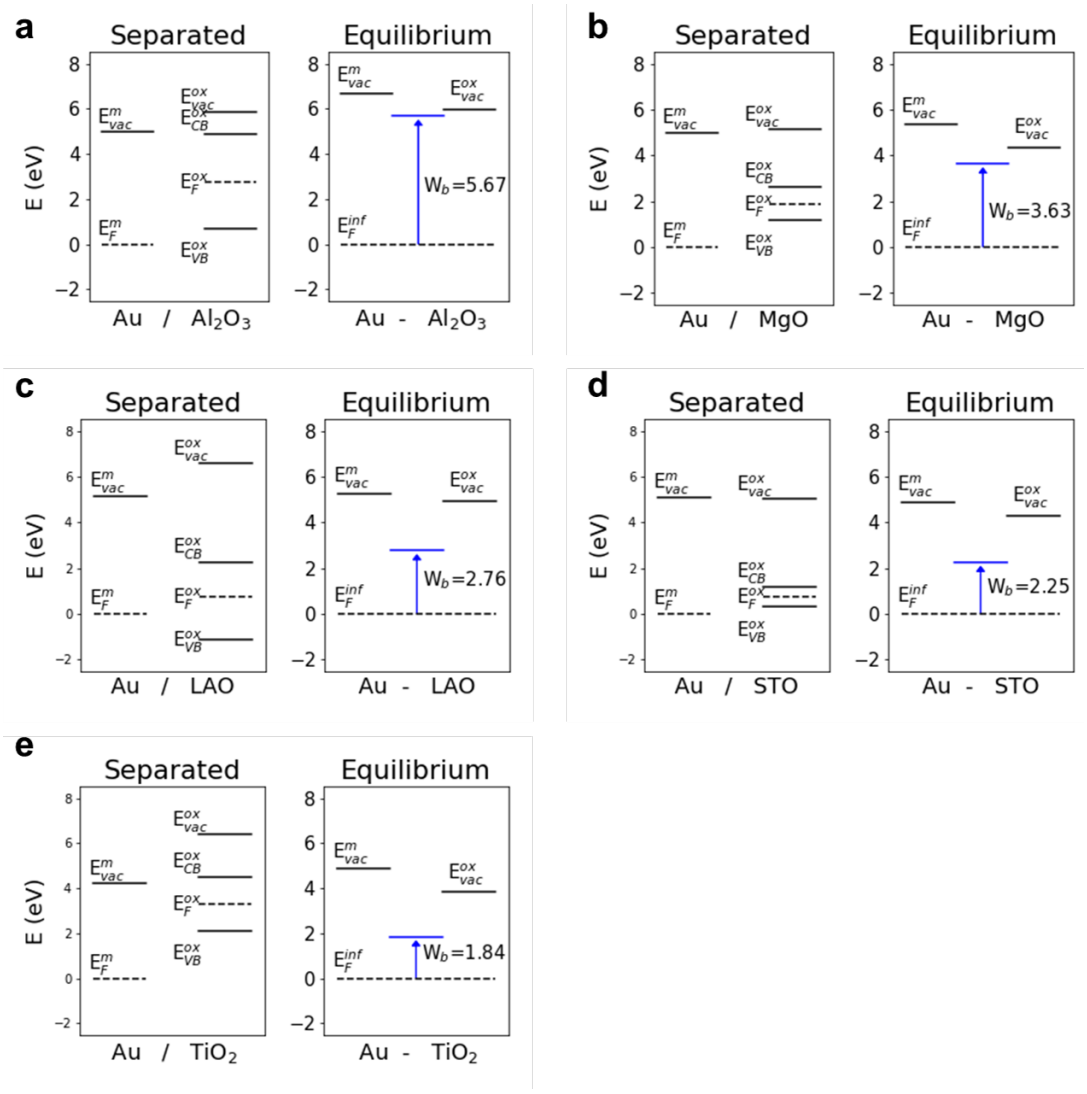


**Figure S6.** (a-e) The energy band diagram before contact (left, separated) and after contact (right, equilibrium) for each Au-dielectric systems: (a) Au-$Al_2O_3$, (b) Au-MgO, (c) Au-$LaAlO_3$, (d) Au-$SrTiO_3$, and (e) Au-$TiO_2$. For the energy level, $E^{m,ox}_{F,vac,VB,CB}$, superscript *m* and *ox* denotes metal and oxide (dielectric), respectively. The subscript F, *vac*, *VB*, and *CB* refers to Fermi energy, vacuum energy, valence band maximum, and conduction band minimum, respectively. The barrier, *W*, calculated from planar averaged electrostatic potential is also plotted for the comparison.

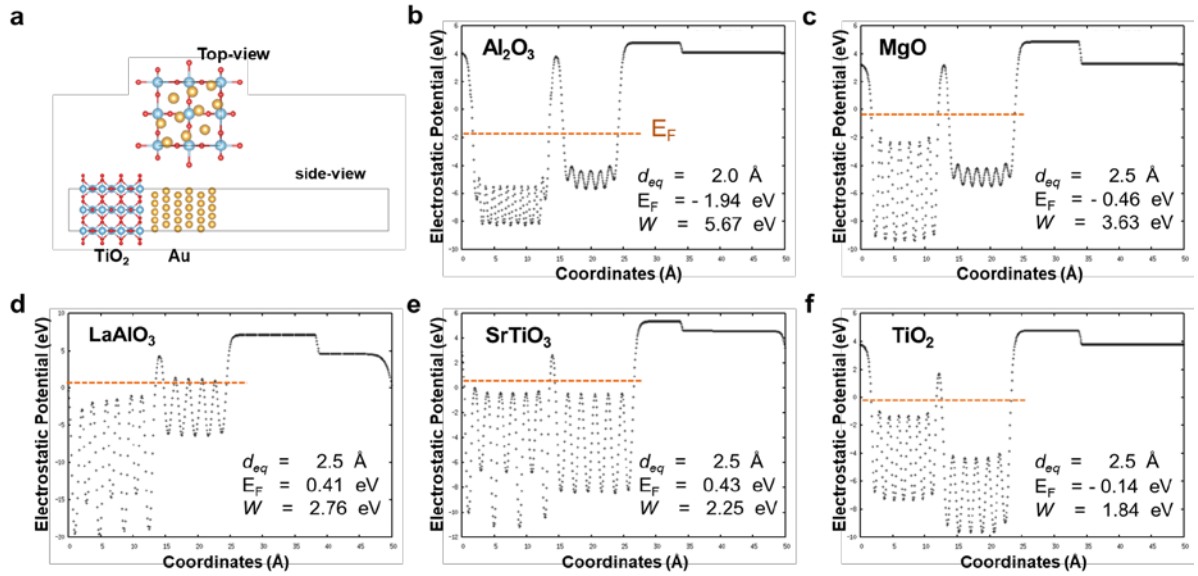


**Figure S7.** The planar averaged electrostatic potentials of Au-dielectric systems. (a) The scheme showing the top- and side-view of the $TiO_2$-Au interface as an example. (b-f) The *z*-axis planar average electrostatic potential for Au-dielectrics, where $d_{eq}$ is the equilibrium distance, $E_F$ is the fermi energy, and *W* is the electrostatic barrier between Au and dielectric.

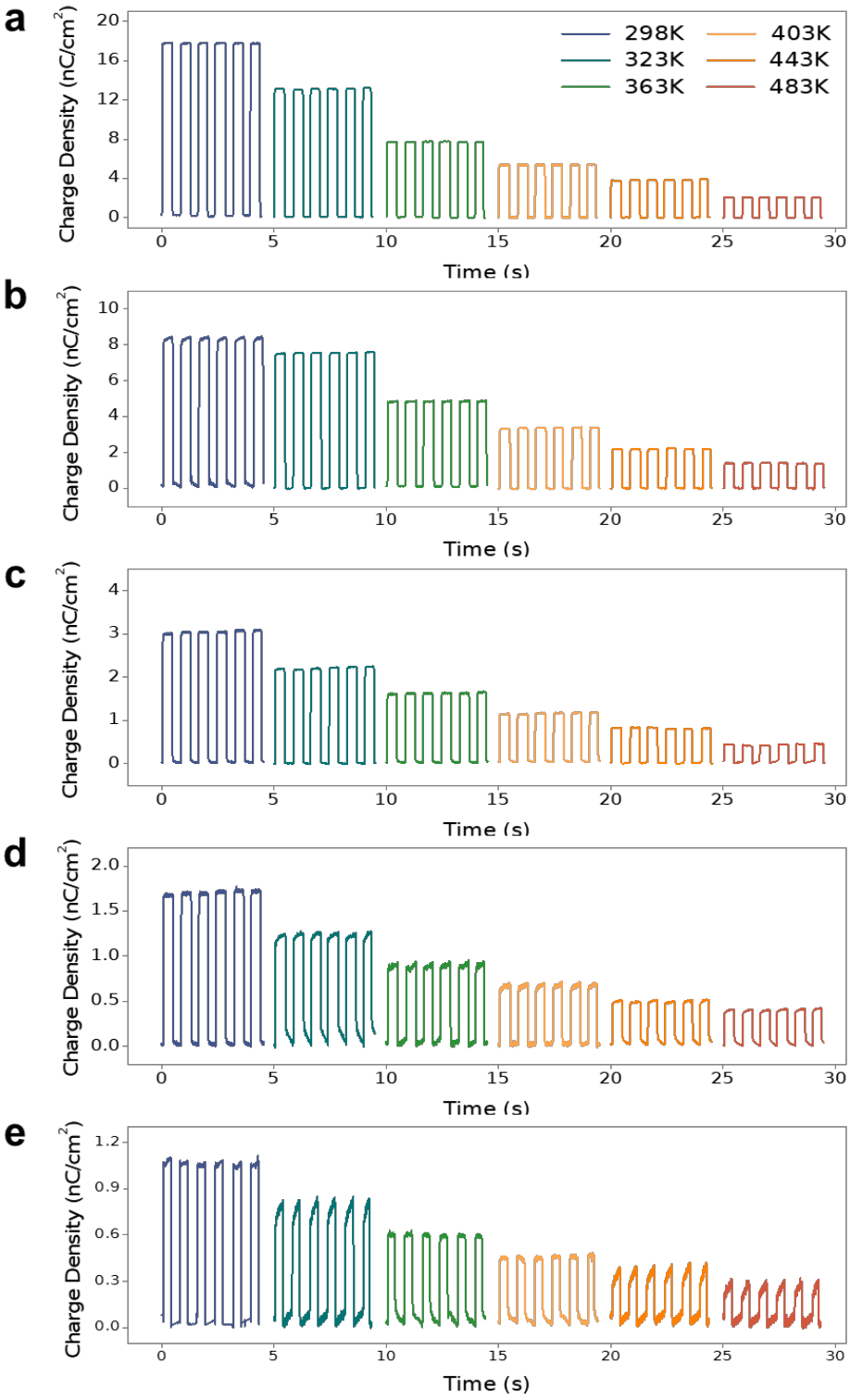


**Figure S8.** (a-e) Electric charge values measured at different temperatures of 298K, 323K, 363K, 403K, 443K and 483K with Au-dielectrics: (a) $Al_2O_3$, (b) MgO, (c) $LaAlO_3$, (d) $SrTiO_3$, (e) $TiO_2$. As the experimental temperature increases, the charge decay occurs in all materials.

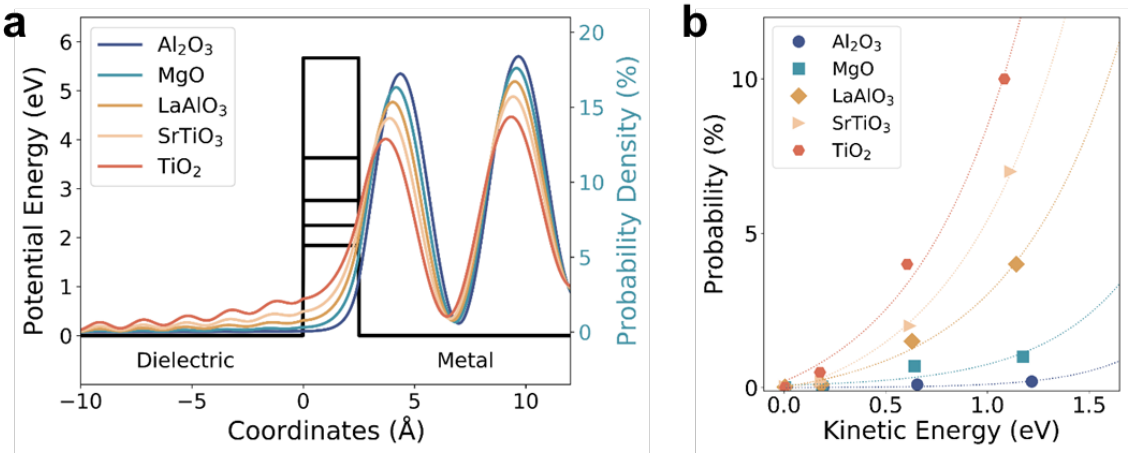


**Figure S9.** (a) Probability density of wave functions with kinetic energy of ~1.1 eV for contact of each metal-dielectric system, with the electron potential energy also shown and square-potential barriers with heights from DFT calculations located between the metal and the dielectric. (b) Tunneling probability as a function of kinetic energy of electrons. Dashed curves are the exponential fitting to the data for each Au-dielectric system.

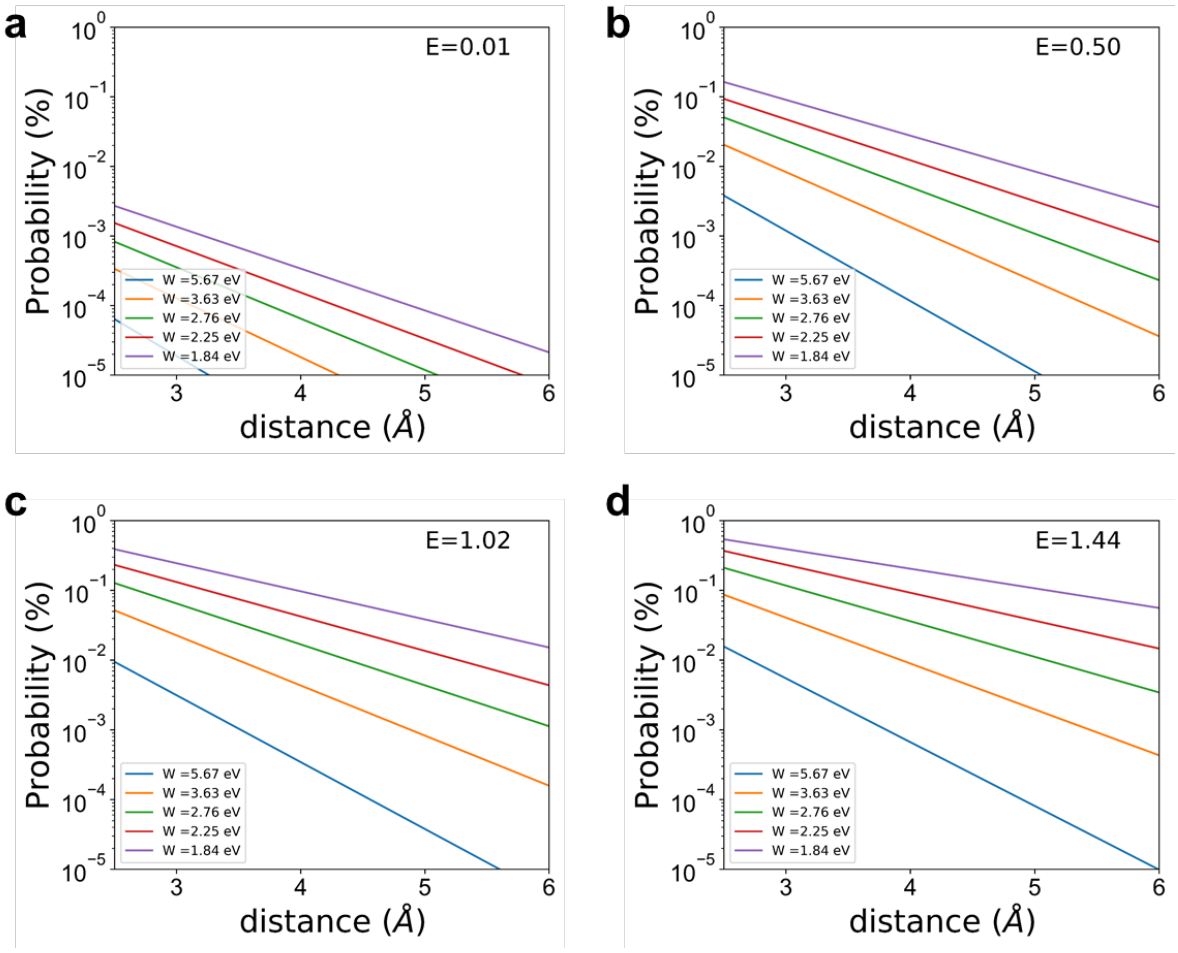


**Figure S10.** (a-d) The barrier-dependent tunneling probability of electrons with kinetic energy of approximately (a) 0.01, (b) 0.50, (c) 1.02, and (d) 1.44 eV.

**Supporting References**

(1) Feng, X.; Li, Q.; Wang, K. Waste Plastic Triboelectric Nanogenerators Using Recycled Plastic Bags for Power Generation. *ACS Appl. Mater. Interfaces* **2021,** *13* (1), 400-410, DOI: 10.1021/acsami.0c16489.
(2) Zhang, C.; Zhou, L.; Cheng, P.; Yin, X.; Liu, D.; Li, X.; Guo, H.; Wang, Z. L.; Wang, J. Surface charge density of triboelectric nanogenerators: Theoretical boundary and optimization methodology. *Appl. Mater. Today* **2020,** *18*, 100496, DOI: 10.1016/j.apmt.2019.100496.
(3) Jiang, C.; Dai, K.; Yi, F.; Han, Y.; Wang, X.; You, Z. Optimization of triboelectric nanogenerator load characteristics considering the air breakdown effect. *Nano Energy* **2018,** *53*, 706-715, DOI: 10.1016/j.nanoen.2018.09.036.
(4) Kresse, G.; Furthmüller, J. Efficiency of ab-initio total energy calculations for metals and semiconductors using a plane-wave basis set. *Comput. Mater. Sci.* **1996,** *6* (1), 15-50.
(5) Kresse, G. From ultrasoft pseudopotentials to the projector augmented-wave method. *Phys. Rev. B* **1999,** *59* (3), 1758, DOI: 10.1103/PhysRevB.59.1758.
(6) Blöchl, P. E. Projector augmented-wave method. *Phys. Rev. B* **1994,** *50* (24), 17953-17979, DOI: 10.1103/PhysRevB.50.17953.
(7) Perdew, J. P.; Burke, K.; Ernzerhof, M. Generalized gradient approximation made simple. *Phys. Rev. Lett.* **1996,** *77* (18), 3865-3868, DOI: 10.1103/PhysRevLett.77.3865.
(8) Neugebauer, J.; Scheffler, M. Adsorbate-substrate and adsorbate-adsorbate interactions of Na and K adlayers on Al(111). *Phys. Rev. B* **1992,** *46* (24), 16067-16080, DOI: 10.1103/PhysRevB.46.16067.
(9) Henkelman, G.; Arnaldsson, A.; Jónsson, H. A fast and robust algorithm for Bader decomposition of charge density. *Comput. Mater. Sci.* **2006,** *36* (3), 354-360.
(10) Michaelson, H. B. The work function of the elements and its periodicity. *J. Appl. Phys.* **1977,** *48* (11), 4729-4733, DOI: 10.1063/1.323539.
(11) Eng, P. J.; Trainor, T. P.; Brown Jr., G. E.; Waychunas, G. A.; Newville, M.; Sutton, S. R.; Rivers, M. L. Structure of the Hydrated α-$Al_2O_3$ (0001) Surface. *Science* **2000,** *288* (5468), 1029-1033, DOI: 10.1126/science.288.5468.1029.
(12) Marmier, A.; Parker, S. C. Ab initio morphology and surface thermodynamics of α −$Al_2O_3$ *Phys. Rev. B* **2004,** *69* (11), 115409, DOI: 10.1103/PhysRevB.69.115409.
(13) Son, W.-j.; Cho, E.; Lee, J.; Han, S. Hydrogen adsorption and carrier generation in LaAlO3–SrTiO3heterointerfaces: a first-principles study. *J. Phys.: Condens. Matter* **2010,** *22* (31), 315501, DOI: 10.1088/0953-8984/22/31/315501.
(14) Yang, Y.; Lin, C.-S.; Cheng, W.-D.; Liu, C.; Liang, T.-X. Origin of H2 Formation on Perfect SrTiO3 (001) Surface: A First-principles Study. *J. Phys. Chem. C* **2018,** *122* (24), 12951-12955, DOI: 10.1021/acs.jpcc.8b03685.
(15) Silveri, F.; Quesne, M. G.; Roldan, A.; de Leeuw, N. H.; Catlow, C. R. A. Hydrogen adsorption on transition metal carbides: a DFT study. *Physical Chemistry Chemical Physics* **2019,** *21* (10), 5335-5343, DOI: 10.1039/C8CP05975F.
(16) Fu, Q.; Wagner, T. Interaction of nanostructured metal overlayers with oxide surfaces. *Surf. Sci. Rep.* **2007,** *62* (11), 431-498, DOI: 10.1016/j.surfrep.2007.07.001.
(17) Xu, C.; Zi, Y.; Wang, A. C.; Zou, H.; Dai, Y.; He, X.; Wang, P.; Wang, Y.-C.; Feng, P.; Li, D.; Wang, Z. L. On the Electron-Transfer Mechanism in the Contact-Electrification Effect. *Adv. Mater.* **2018,** *30* (15), 1706790, DOI: 10.1002/adma.201706790.
(18) Cho, S. B.; Yun, K.-H.; Yoo, D. S.; Ahn, K.; Chung, Y.-C. Work function tuning of an ultrathin MgO film on an Ag substrate by generating oxygen impurities at the interface. *Thin Solid Films* **2013,** *544*, 541-544, DOI: 10.1016/j.tsf.2012.12.072.
(19) Prada, S.; Martinez, U.; Pacchioni, G. Work function changes induced by deposition of ultrathin dielectric films on metals: A theoretical analysis. *Phys. Rev. B* **2008,** *78* (23), 235423, DOI: 10.1103/PhysRevB.78.235423.

(20) Cowley, A. M.; Sze, S. M. Surface States and Barrier Height of Metal-Semiconductor Systems. *J. Appl. Phys.* **1965,** *36* (10), 3212-3220, DOI: 10.1063/1.1702952.
(21) Lowell, J.; Rose-Innes, A. C. Contact electrification. *Adv. Phys.* **1980,** *29* (6), 947-1023, DOI: https://doi.org/10.1080/00018738000101466.
(22) Ernst, L. Optical spectroscopy of surface states on NaCl and KCl crystals and its relation to contact charging. *Solid State Commun.* **1976,** *19* (4), 311-314, DOI: https://doi.org/10.1016/0038-1098(76)91339-9.
(23) Kittaka, S.; Murata, Y. Photoelectric Emission and Contact Charging of Vacuum-UV Irradiated Polymers. *Jpn. J. Appl. Phys.* **1979,** *18* (3), 515-521, DOI: https://doi.org/10.1143/jjap.18.515.
(24) Lacks, D. J.; Duff, N.; Kumar, S. K. Nonequilibrium Accumulation of Surface Species and Triboelectric Charging in Single Component Particulate Systems. *Phys. Rev. Lett.* **2008,** *100* (18), 188305, DOI: https://doi.org/10.1103/PhysRevLett.100.188305.
(25) Antony, A. C.; Thelen, D.; Zhelev, N.; Adib, K.; Manley, R. G. Electronic charge transfer during metal/SiO2 contact: Insight from density functional theory. *J. Appl. Phys.* **2021,** *129* (6), 065304, DOI: https://doi.org/10.1063/5.0038302.
(26) Mizzi, C. A.; Lin, A. Y. W.; Marks, L. D. Does Flexoelectricity Drive Triboelectricity? *Phys. Rev. Lett.* **2019,** *123* (11), 116103, DOI: https://doi.org/10.1103/PhysRevLett.123.116103.
(27) Chen, L.; Shi, Q.; Sun, Y.; Nguyen, T.; Lee, C.; Soh, S. Controlling Surface Charge Generated by Contact Electrification: Strategies and Applications. *Adv. Mater.* **2018,** *30* (47), 1802405, DOI: https://doi.org/10.1002/adma.201802405.
(28) Fatti, G.; Righi, M. C.; Dini, D.; Ciniero, A. Ab Initio Study of Polytetrafluoroethylene Defluorination for Tribocharging Applications. *ACS Appl. Polym. Mat.* **2020,** *2* (11), 5129-5134, DOI: https://doi.org/10.1021/acsapm.0c00911.
(29) Zhang, Y.; Shao, T. Effect of contact deformation on contact electrification: a first-principles calculation. *J. Phys. D: Appl. Phys.* **2013,** *46* (23), 235304, DOI: https://doi.org/10.1088/0022-3727/46/23/235304.
(30) Chiu, F.-C. A Review on Conduction Mechanisms in Dielectric Films. *Adv. Mater. Sci. Eng.* **2014,** *2014*, 578168, DOI: https://doi.org/10.1155/2014/578168.
(31) Franciosi, A.; Van de Walle, C. G. Heterojunction band offset engineering. *Surf. Sci. Rep.* **1996,** *25* (1), 1-140, DOI: https://doi.org/10.1016/0167-5729(95)00008-9.
(32) Yeo, Y.-C.; King, T.-J.; Hu, C. Metal-dielectric band alignment and its implications for metal gate complementary metal-oxide-semiconductor technology. *J. Appl. Phys.* **2002,** *92* (12), 7266-7271, DOI: https://doi.org/10.1063/1.1521517.
(33) Zhong, Z.; Hansmann, P. Band Alignment and Charge Transfer in Complex Oxide Interfaces. *Phys. Rev. X* **2017,** *7* (1), 011023, DOI: https://doi.org/10.1103/PhysRevX.7.011023.
(34) Greiner, M. T.; Chai, L.; Helander, M. G.; Tang, W.-M.; Lu, Z.-H. Metal/Metal-Oxide Interfaces: How Metal Contacts Affect the Work Function and Band Structure of MoO3. *Adv. Funct. Mater.* **2013,** *23* (2), 215-226, DOI: 10.1002/adfm.201200993.